iScience

CellPress
OPEN ACCESS

Article

Self-evolved BO_x anchored on $Mg_2B_2O_5$ crystallites for high-performance oxidative dehydrogenation of propane

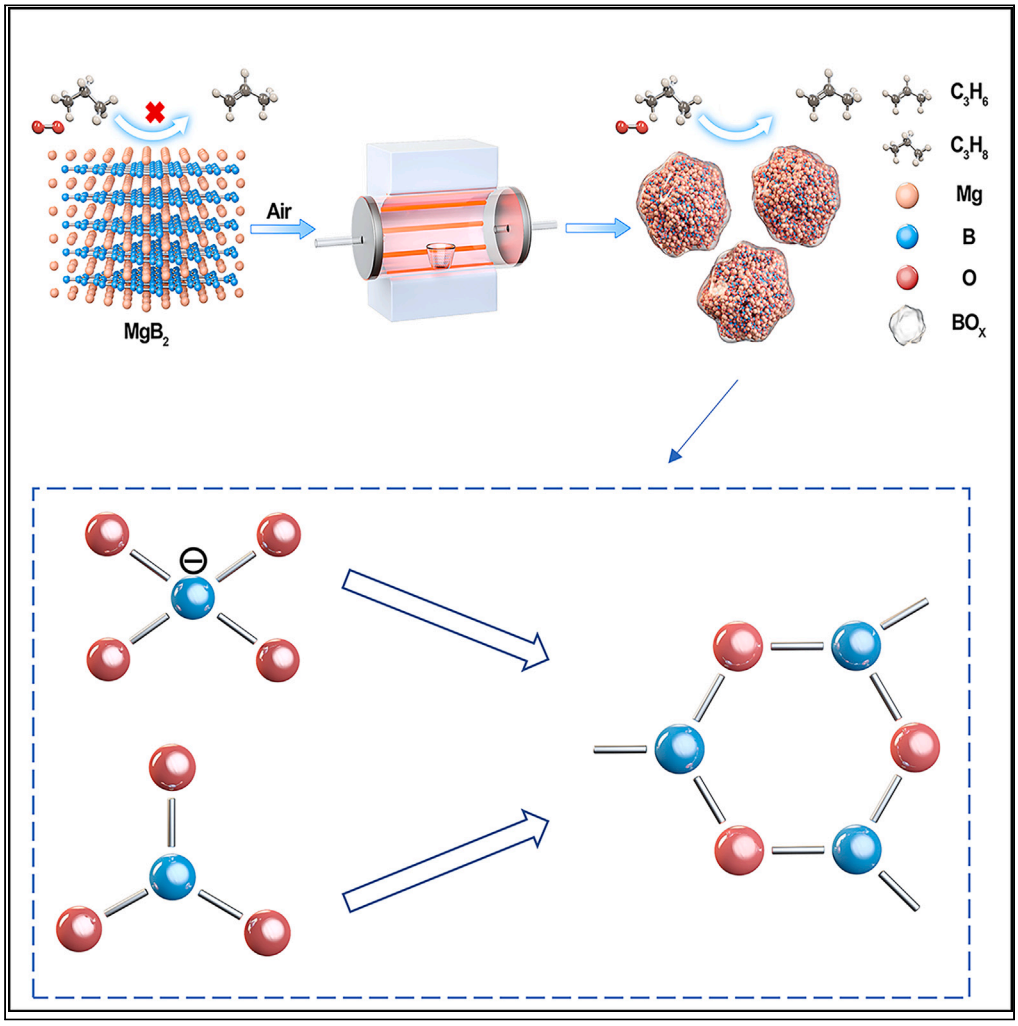

Dake Zhang, Shenghua Wang, Xingyu Lu, ..., Hui Zhang, Wei Sun, Deren Yang

sunnyway423@zju.edu.cn (W.S.)
mseyang@zju.edu.cn (D.Y.)

Highlights

A self-evolution method is developed to acquire catalytic structures from MgB_2

The catalyst is ultra-stable for high-throughput oxidative dehydrogenation of propane

The catalyst exhibits 60% propane conversion with 43.2% olefin yield at 535°C

The BO_x corona pinned by borate contains B-O rings as the highly active sites

Zhang et al., iScience 26, 108135
November 17, 2023
https://doi.org/10.1016/j.isci.2023.108135

iScience

CellPress
OPEN ACCESS

Article

Self-evolved BO_x anchored on $Mg_2B_2O_5$ crystallites for high-performance oxidative dehydrogenation of propane

Dake Zhang,[1] Shenghua Wang,[1] Xingyu Lu,[2] Chengcheng Zhang,[3] Kai Feng,[3] Le He,[3] Hui Zhang,[4] Wei Sun,[1,5,*] and Deren Yang[1,*]

SUMMARY

Oxidative dehydrogenation of propane (ODHP) is a promising process for producing propene. Recently, some boron-based catalysts have exhibited excellent olefin selectivity in ODHP. However, their complex synthetic routes and poor stability under high-temperature reaction conditions have hindered their practical application. Herein, we report a self-evolution method rather than conventional assembly approaches to acquire structures with excellent stability under a high propane conversion, from a single precursor—MgB_2. The catalyst feasibly prepared and optimized exhibited a striking performance: 60% propane conversion with a 43.2% olefin yield at 535°C. The BO_x corona pinned by the strong interaction with the borate enabled zero loss of the high conversion (around 40%) and olefins selectivity (above 80%) for over 100 h at 520°C. This all-in-one strategy of deriving all the necessary components from just one raw chemical provides a new way to synthesize effective and economic catalysts for potential industrial implementation.

INTRODUCTION

Propene is an essential raw material for many fine chemical products. Nowadays, the primary technology of propene production depends on steam cracking of oil-derived naphtha.[1–3] In addition, utilizing the low-cost shale gas, which contains abundant amount of propane, to produce propene by direct dehydrogenation is also an effective route.[4–7] However, these processes suffer from obvious disadvantages, such as high reaction temperature, coke formation, and frequent regeneration of catalysts.

The oxidative dehydrogenation of propane (ODHP) has emerged as a promising alternative way to gain propene owing to its exothermic nature, low operative temperature, and coke-resistant feature.[8,9] Compared with transition metal oxides catalysts (e.g., V_2O_5,[10] V-MgO,[11] $NiMoO_4$[12]) that often yield significant portion of the unwanted by-products CO and CO_2, the state-of-the-art ODHP catalysts that often incorporate boron have exhibited much improved selectivity to olefins. Hexagonal boron nitride (h-BN) can exemplify such novel catalysts and has attracted considerable attention.[9,13] Recently, a number of spectral experiments and calculations have proved that BO_x/B-$(OH)_xO_{3-x}$ species are actually the active sites, which are derived from h-BN under the high-temperature and oxygen-abundant ODHP reaction process.[14,15] However, these active species suffer from leaching when working toward high olefin yield, due to the hot and water-rich environment.[16,17] Facing this issue, it usually takes extra effort in the process or deliberate design of the catalyst to stabilize the active sites. For example, Chaturbedy et al. reported that the addition of the reductive agent ammonia in the reaction feed would alleviate overoxidation of h-BN and enhance the catalytic stability from 5 h to 100 h over ODHP at 540°C.[18] In another recent work, Cao et al. constructed h-BN⊃xIn_2O_3 composite catalysts through the atomic layer deposition (ALD) process for ODHP, which improved the catalytic stability nearly five times than pristine h-BN owing to the strong metal oxide-support interaction (SMOSI) effect between In_2O_3 and h-BN that could derive a BO_x thin layer around the metal oxide.[19] Nevertheless, some important issues of these brilliant catalysts cannot be ignored, such as the complex synthesis route and high-price raw materials, which are not conducive to practical application. Therefore, it is urgent but still a great challenge to explore new materials with high activity and stability for ODHP that can be synthesized with a simple method.

Targeting this challenge, we endow a commercial raw material with excellent activity and stability by simply utilizing the direct oxidative transition of MgB_2, an established boron-containing chemical well known as a low-cost superconductor material and fuel for rocket

[1]State Key Laboratory of Silicon Materials and Advanced Semiconductor Materials, School of Materials Science and Engineering, Zhejiang University, Hangzhou, Zhejiang 310027, People's Republic of China
[2]Key Laboratory of Precise Synthesis of Functional Molecules of Zhejiang Province, Instrumentation and Service Center for Molecular Sciences, Westlake University, 18 Shilongshan Road, Hangzhou 310024, Zhejiang Province, China
[3]Institute of Functional Nano and Soft Materials (FUNSOM), Jiangsu Key Laboratory for Carbon-Based Functional Materials and Devices, Soochow University, Suzhou 215123, Jiangsu, China
[4]Zhejiang Provincial Key Laboratory of Power Semiconductor Materials and Devices, ZJU-Hangzhou Global Scientific and Technological Innovation Center, Hangzhou, Zhejiang 311200, People's Republic of China
[5]Lead contact
*Correspondence: sunnyway423@zju.edu.cn (W.S.), mseyang@zju.edu.cn (D.Y.)
https://doi.org/10.1016/j.isci.2023.108135

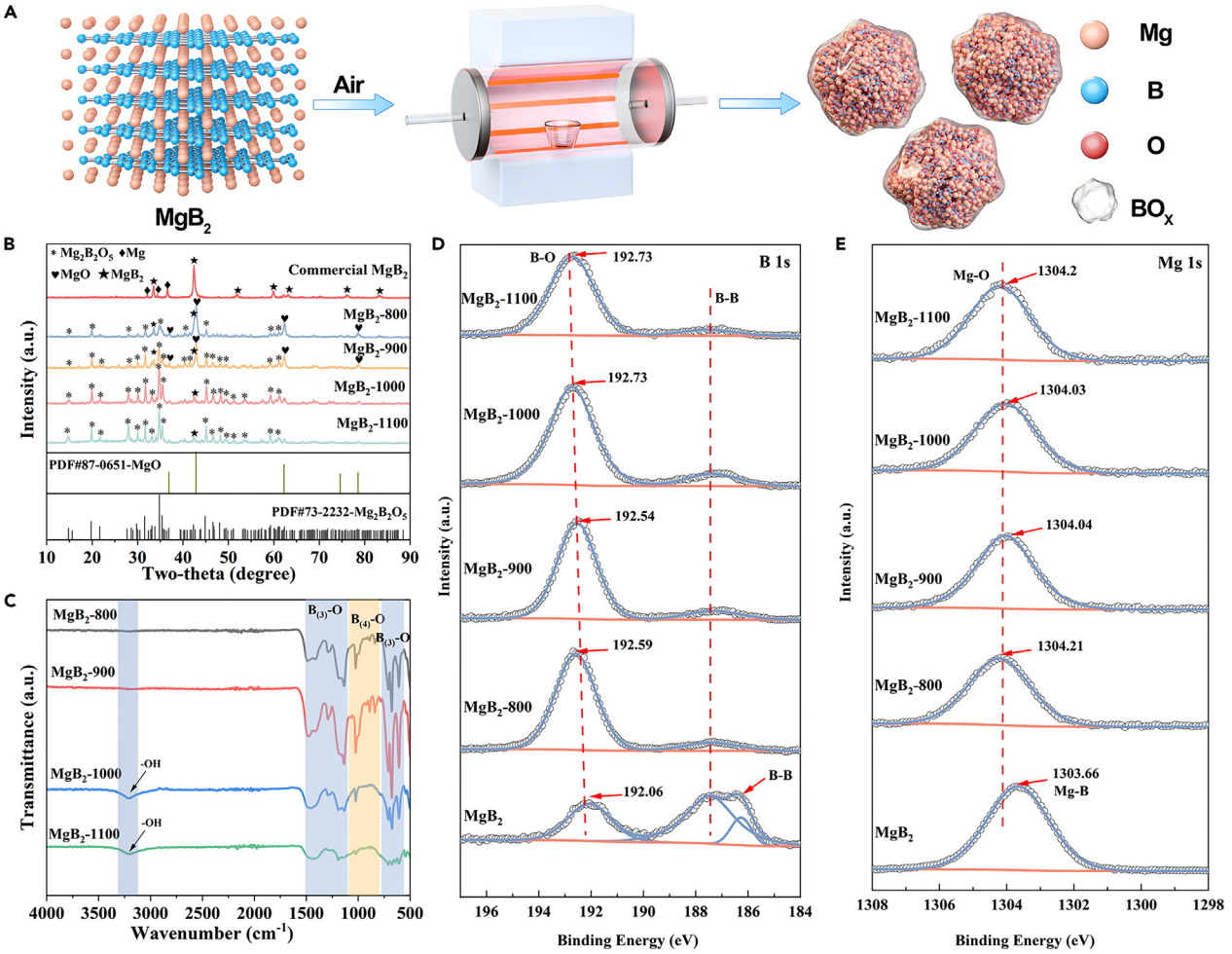

Figure 1. Schematic illustration and structure characterizations

(A) Schematic showing the fabrication process of MgB_2-x.

(B) XRD patterns of commercial MgB_2 and MgB_2-x.

(C) FT-IR spectra of MgB_2-x.

(D) XPS results of B 1s.

(E) XPS results of Mg 1s.

propulsion. After just a single step of calcination at 1000°C, the originally non-catalytic MgB_2 as the sole precursor evolved into a high-performance catalyst. Upon oxidation at the high temperature, amorphous BO_x was *in situ* generated, which is pinned by $Mg_2B_2O_5$, exhibiting excellent stability in a prolonged test under the high-throughput working condition. With a simple etching step, the surface area of the catalyst was further enhanced nearly 15 times, fostering an excellent and stable performance under the harsh working condition for high yield: 60% propane conversion and a 43.2% olefin yield at 535°C. Our study clearly demonstrates that highly efficient ODHP process may not always need exquisite synthesis or regeneration of the catalysts—the simplicity of oxidizing borides endows this effective strategy with even higher potential for industrialization.

RESULTS AND DISCUSSION

MgB_2 is an ionic compound, which has a unique structure with intercalated layers of Mg and B. It is worth noting that the MgB_2 as received was inactive for ODHP at 520°C (Figure S1A), because there were no BO_x/B-$(OH)_xO_{3-x}$ species, which have been considered as the active centers for ODHP.[20,21] The thermogravimetric analysis (TG) of MgB_2 indicated its stability against oxidation below 600°C (Figure S1B).

As illustrated in Figure 1A, the self-evolved high-performance boron-based catalysts were prepared by oxidation of a metal boride MgB_2. The MgB_2 was calcined at higher temperatures of 800°C–1100°C for 3h in air (denoted MgB_2-x, where x represents the calcination temperature). As illustrated in the X-ray diffraction (XRD) patterns in Figure 1B, the commercial powder mainly consists of MgB_2 and a bit of Mg as the impurity. After calcination at 800°C and 900°C, the MgB_2 underwent a transition upon oxidation, and $Mg_2B_2O_5$ and MgO crystallites were

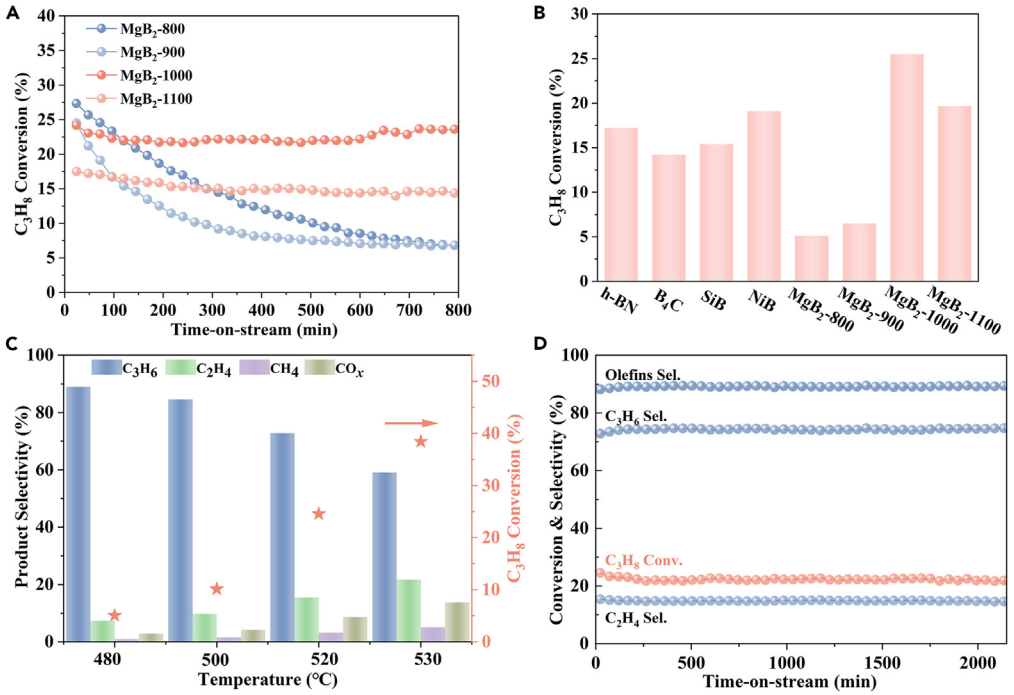

Figure 2. Catalytic performance

(A) Long-time conversions of the MgB_2-x samples at 520°C tested for 800 min.

(B) The stabilized conversions of the boron-based catalysts at 520°C.

(C) Catalytic performance of MgB_2-1000 at different temperatures.

(D) Stability test of MgB_2-1000 at 520°C for 35 h. Reaction conditions for the flow tests: atmospheric pressure, $C_3H_8/O_2/N_2$ ratio = 6:3:11, WHSV = 12000 mL/g/h.

observed, with a slight amount of MgB_2 retained. When the calcination temperature reached 1000°C and above, $Mg_2B_2O_5$ was the main crystalline phase observed. Meanwhile, the Fourier transform infrared spectroscopy (FT-IR) spectra of the catalysts are shown in Figure 1C. Compared with the FT-IR spectrum of MgB_2 (Figure S2), the samples calcined at high temperatures had more boron-oxygen species. The peaks between 1,490 cm^{-1} and 1,140 cm^{-1} were all ascribed to the stretching vibrations of the three-coordinate boron ($B_{(3)}$-O). Four-coordinate boron ($B_{(4)}$-O) was also observed in the range between 1,100 cm^{-1} and 800 cm^{-1}. The presence of MgO would change the boron coordination from three to four, so MgB_2-800 and MgB_2-900 had more ($B_{(4)}$-O) than MgB_2-1000 and MgB_2-1100. The transmission peaks in the 608-712 cm^{-1} range corresponded to the bending mode of three-coordinate boron ($B_{(3)}$-O).[22,23] It is worth noting that MgB_2-1000 and MgB_2-1100 had the obvious O-H mode at 3,200 cm^{-1} but MgB_2-800 and MgB_2-900 did not. As illustrated in Figure 1D, two B species are indicated in the B 1s spectra: one in B-O bond (>192 eV), the other in B-B bond (<190 eV).[24–26] Compared with B 1s of MgB_2, the B-O bonds of MgB_2-x shifted to higher binding energies. Meanwhile, the B-B bonds almost disappeared when the MgB_2 was subjected to heating at elevated temperatures. As shown in Table S1, the content results of each B 1s functional groups further confirmed that B-B bonds have transformed to B-O bonds upon high temperature oxidation. The MgB_2-1100 has the highest content ratio of B-O/B-B but also suffered from B loss. In addition, the Mg 1s peak shifted from 1303.66 eV (Mg-B) to 1304.03–1304.20 eV (Mg-O) (Figure 1E).[27,28] These results confirmed that MgB_2 itself has evolved with abundant B-O sites which are beneficial for the follow-up catalytic tests over ODHP.

The prepared materials were tested for ODHP without any further activation. Meanwhile, for the sake of fair comparison with existing catalysts, the commercial h-BN and other boron-based materials that have been reported to be active for ODHP were tested under the equivalent reaction conditions. The propane conversion of blank (without catalyst) was below 2.0%, which proved there was barely any spontaneous reaction between propane and oxygen at 540°C (Figure S3). Figure 2A and Figure S4 show the long-time conversions of the various catalysts at 520°C. Compared with MgB_2-800 and MgB_2-900 of which the conversion quickly dropped below 7% within 800 min, the MgB_2-1000 and MgB_2-1100 catalysts exhibited excellent catalytic stability during the test. The commercial h-BN exhibited the initial propane conversion of 30% at 520°C, but it slowly decreased to 17% over a run time of 10 h, corresponding well with the catalytic activity decay also observed in the previous works.[8,19] The presence of H_3BO_3 was evidenced by XRD in the spent h-BN (Figure S5), which could account for the instability since H_3BO_3 would be leached into a humid atmosphere. As to other common boron-containing catalysts, the propane conversion of B_4C was stabilized at 14% after 10 h, and with a short activation period, 15% and 19% of propane conversions were observed on SiB and NiB, respectively. Compared with all these boron-containing compound catalysts including the extensively studied h-BN, MgB_2-1000 catalyst exhibited the highest propane conversions of around 25% at 520°C (Figure 2B). Furthermore, the ODHP performance of the best long-term performer MgB_2-1000 as a function of reaction temperature (480°C–530°C) was evaluated (Figure 2C). The propane conversion of 5% was observed

at the relatively low temperature of 480°C, while the selectivities of propene and ethylene were as high as 88.9% and 7.25%, respectively. The propane conversion increased with the reaction temperature. A record-high propane conversion of 38.4% was achieved for the MgB_2-1000 catalysts at 530°C. The excellent stability of the best performer MgB_2-1000 in terms of both conversion and selectivity was further manifested at 520°C for a prolonged period of 35 h (Figure 2D). The propane conversion was maintained at around 23% and the selectivity of olefins (propene and ethylene) at around 89%. Meanwhile, the carbon balance stayed at 100 $\pm$ 2% during the test (Figure S6). These results indicated the self-evolution of MgB_2 was an effective strategy to construct high-performance boron-based catalysts for ODHP.

The high activity and stability of MgB_2-1000 catalyst motivated us to further explore the effect of oxidation temperature. As shown in Figure S7, the boron contents of the catalysts were measured by an inductively coupled plasma optical emission spectroscopy (ICP-OES). The MgB_2-800 sample had 30.3% boron content. However, with the calcination temperature increases, the overall boron content decreases. This is due to the evaporation of boron under the high-temperature condition.[29] Therefore, the MgB_2-1100 catalyst has the lowest initial catalytic activity than the other samples. Next, we explored the possible reasons that might cause the discrepancy in the long-term catalytic performance of the samples prepared at different temperatures. TG of the tested MgB_2-800 with the poorest stability confirms that there was no coke formation (Figure S8). Meanwhile, The XRD patterns and FT-IR spectra of the tested samples do not distinguish from those of the fresh catalysts (Figures S9A and S9B). In addition, the Mg 1s and B 1s XPS results of the tested catalysts indicate the positions of the surface Mg-O and B-O species were almost unchanged (Figures S10A and S10B). However, there is an obvious reduction in the boron content after the long catalytic reaction compared with the fresh samples for MgB_2-800 and MgB_2-900 (Figure S7). This corresponds well with their poor stability. We speculate some weakly bound boron escaped from their surface under the harsh reaction conditions. The scanning electron microscopy (SEM) images (Figure S11) indeed show MgB_2-800 and MgB_2-900 have more collapsed morphologies with plenty of debris, while MgB_2-1000 and MgB_2-1100 appear with bulky structures that are more tightly bonded. In order to confirm this speculation, as shown in Figure S12, we intentionally treated the catalysts with water before the catalytic test. Expectedly, MgB_2-800 and MgB_2-900 exhibited significantly lower propane conversions at around 4% and 10% at 520°C with this treatment, respectively. By contrast, MgB_2-1000 after the water treatment exhibited a 23% propane conversion, which is similar with its untreated form and a good stability over 30 h at 520°C (Figure S13). Therefore, we speculate that during the phase transition of MgB_2 under high-temperature conditions, a stable phase containing surface boron species is formed when the calcination temperature exceeds 1,000°C. To supplement, prolonging the calcination time at 1,000°C does not affect the performance (Figure S14), so temperature is still the determining parameter.

Considering that the XRD pattern of MgB_2-1000 indicates the main crystalline phase is $Mg_2B_2O_5$ (Figure 1B), we prepared pure $Mg_2B_2O_5$ phase via the reported coprecipitation and sintering process, to evaluate its catalytic performance. As shown in Figure S15, the SEM image of $Mg_2B_2O_5$ shows it is mainly composed with smooth, straight nanowires. The TEM and elemental mapping images reveal the uniform distribution of Mg, B, and O (Figure S16). All of the diffraction peaks fit well with $Mg_2B_2O_5$ (PDF#73–2232), and the FT-IR spectrum of $Mg_2B_2O_5$ nanowires is consistent with MgB_2-1000 without OH, with abundant B-O vibrational bands (Figures S17A and S17B). However, $Mg_2B_2O_5$ nanowires were almost inactive for ODHP, with the propane conversion below 2% at 520°C (Figure S18). Therefore, it is concluded that the phase of $Mg_2B_2O_5$ was not the active center.

While XRD could easily reveal the crystalline phase of $Mg_2B_2O_5$, it could not show the amorphous phase. Therefore, we further studied the structure of MgB_2-1000 under electron microscopes to explore the real active sites. As shown in Figure 3A, a layer of amorphous structure is located on the surface of MgB_2-1000. Meanwhile, TEM and HRTEM (high resolution transmission electron microscope) images in Figure 3B confirm that MgB_2-1000 is actually composed of both crystalline and amorphous components. The lattice spacing of the crystalline area of MgB_2-1000 in the HRTEM image was measured to be 0.269 nm that corresponds to the (1 -1 1) plane of $Mg_2B_2O_5$. The selective area diffraction patterns (SAED) also confirmed the presence of both crystalline and amorphous areas in MgB_2-1000. Elemental mapping analysis of MgB_2-1000 (Figures 3C–3E) reveals that the amorphous phase is mainly composed of B and O. According to these characterization results, we speculate the crystalline $Mg_2B_2O_5$ was wrapped by a layer of amorphous BO_x, forming a typical strong-interaction structure, similar with the SMOSI structure that has been recently observed between metal oxides (e.g., In_2O_3) and BO_x layer.[19] The difference is that we constructed a metal boride instead of a metal oxide to pin the BO_x outer layer under the high-temperature condition. As discussed earlier, significant amount of MgO (seen in XRD patterns) and boron oxide (seen in IR and XPS patterns) were produced when MgB_2 was oxidized at the relatively lower temperatures of 800°C and 900°C: $MgB_2 + 2O_2 \rightarrow MgO + B_2O_3$; at the meantime and especially when subjected to higher temperature heating at 1,000°C and 1,100°C, MgO evolved into $Mg_2B_2O_5$: $2MgO + B_2O_3 \rightarrow Mg_2B_2O_5$, leaving the rest of the surface boron oxide species as the corona of BO_x seen in the TEM images.[30] Given that the pure $Mg_2B_2O_5$ is not active for ODHP but MgB_2-1000 is, we speculate that the BO_x which is the extra phase, should be the active site for ODHP. Moreover, inspired by the mechanism that metal oxide can stabilize BO_x (derived from BN) through the SMOSI pinning effect,[19] we can attribute the excellent stability of MgB_2-1000 to the similar strong interaction. Moreover, the metal borate ($Mg_2B_2O_5$) in this system performed even better than the metal oxide (MgO) in stabilizing BO_x, as discussed about the long-term performance comparison between MgB_2-800/900 and MgB_2-1000/1100.

In addition, the difference in the intensity of hydroxyl group observed in the FTIR spectra also gave us the clue that stably supported BO_x is present in MgB_2-1000 (Figure 1C). Therefore, the thermal gravimetric with mass spectroscopy (TG-MS) analyses of the catalysts were conducted under N_2 atmosphere. As illustrated in Figure 4A, the results reveal that MgB_2-800 and MgB_2-900 did not undergo -OH loss during the process of programmed heating. However, the masses of MgB_2-1000 and MgB_2-1100 decreased and then the -OH and H_2O signals were observed between 100°C and 200°C. These results indicate MgB_2-1000 and MgB_2-1100 indeed have more -OH on the surface than MgB_2-800 and MgB_2-900. Therefore, we speculate that more well-supported BO_x sites were exposed after the calcination above 1,000°C and obtained -OH in air. Meanwhile, the TG-MS results of the different samples under O_2 atmosphere had the same trend (Figure S19).

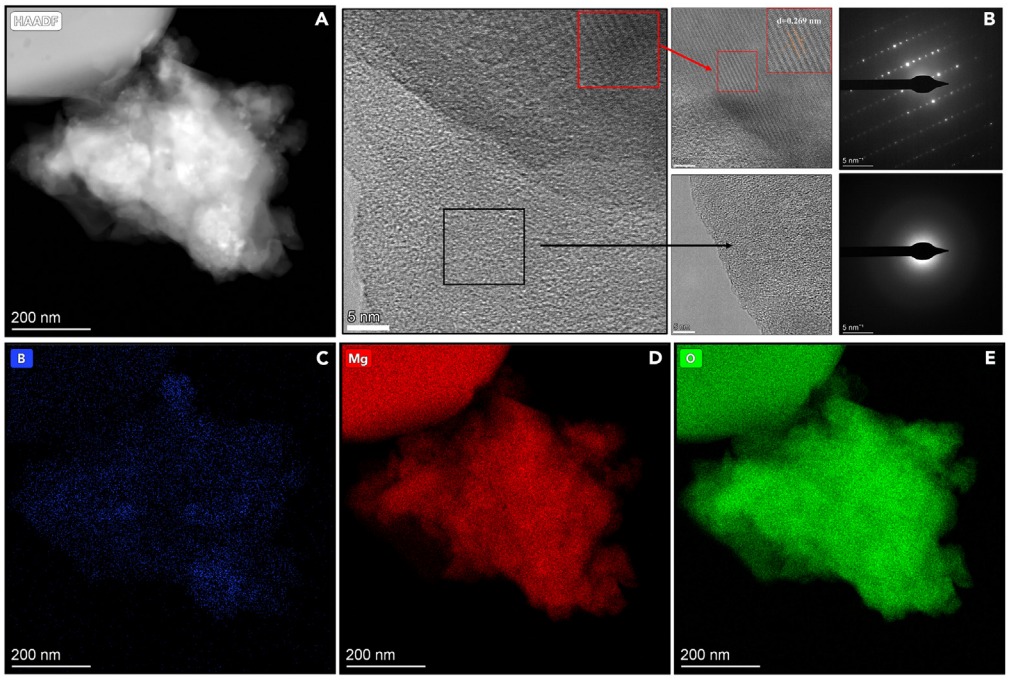

Figure 3. Microscopic characterizations of MgB_2-100

(A) High-angle annular dark-field (HAADF) image.

(B) High-resolution TEM (transmission electron microscope) images and selected area diffraction patterns.

(C–E) The EDS (energy dispersive spectroscopy) mapping images of B, Mg, and O.

Furthermore, a control sample (B_2O_3/MgO) was prepared by impregnating B_2O_3 (30 wt %) onto MgO (70 wt %) to verify the active component. As shown in Figure S20A, the main phase of B_2O_3/MgO was MgO, but weak signals of amorphous phases were also observed, which were ascribed to boron oxides. However, when the impregnation was conducted with a relatively high calcination temperature of 800°C (B_2O_3/MgO-800), the abundant MgO would react with B_2O_3 and turned all of it into the $Mg_2B_2O_5$ phase. The IR results also show the broad B-O stretching modes of B_2O_3 have changed to the distinct modes corresponding with $Mg_2B_2O_5$ in B_2O_3/MgO-800 (Figure S20B). The catalytic test results show a 9% propane conversion was obtained at 520°C over B_2O_3/MgO, but B_2O_3/MgO-800 was almost inactive for ODHP, with the propane conversion of only around 2% at 520°C (Figure S20C). Meanwhile, the propane conversion of pristine MgO was also below 2%. Therefore, these results further confirmed that $Mg_2B_2O_5$ originated from MgO, but neither of these two species were the active center, and the amorphous boron oxide was instead the real active site for ODHP. Note that the coarsely supported B_2O_3 through this traditional impregnation method performed much worse than our MgB_2-1000, further demonstrating the superiority of our strategy of obtaining self-evolved structure and the BO_x sites directly from a single precursor MgB_2.

To better understand the active sites, kinetic studies were conducted to get insights into the reaction pathway of ODHP over MgB_2-1000 (Figures 4B and 4C). The reaction rate of propane consumption increased with the O_2 pressure, but the dependence became weaker at higher O_2 pressure. The results were consistent with the reported model proposed by Hermans et al.[9] and Lu et al.,[31] in which O_2 is adsorbed on the BO_x sites for further reaction. Meanwhile, a near second-order dependence of propane concentration indicated that the propane oxidation occurs between the gaseous propane and the activated oxygen species on the BO_x sites (Figure S21). In addition, the C2 selectivities are higher than C1 (C2/C1>2) at different temperatures over MgB_2-1000 catalyst (Figure 2C), indicating there also exists gas-phase reaction routes, such as the oxidative coupling of methyl. Such reaction pathway and evidence were also observed in other boron-based catalysts at high temperature.[32–35]

For the sake of further improving the catalytic performance and revealing the features of the real active sites BO_x, we explored the effect of a simple treatment of MgB_2-1000 with HCl (denoted as MgB_2-1000-HCl), which can corrode $Mg_2B_2O_5$. Figure S22A and S22B show the stark color contrast before and after etching, which indicates the evolution of structure. After HCl treatment, the material was almost amorphous, and the previously evident signal of the $Mg_2B_2O_5$ phase became weak in the XRD pattern (Figure S23). The HRTEM image in Figure S24 revealed that the MgB_2-1000-HCl was a mixture of amorphous/crystalline phases. EDS element mapping images of MgB_2-1000-HCl indicated the relatively uniform distribution of Mg, B, and O (Figure S25). XPS survey spectrum further confirmed the MgB_2-1000-HCl mainly contains Mg, B, and O (Figure S26). These results confirmed that the MgB_2-1000-HCl was composed by abundant amorphous BO_x and slight amount of crystalline $Mg_2B_2O_5$. In addition, the SEM images of MgB_2-1000-HCl showed the obvious rough and porous morphology, distinct from the smooth structure of MgB_2-1000 without treatment (Figure S27). Interestingly, the presence of B-H stretching vibrations at 1,617 cm^{-1} in the FTIR data was observed for MgB_2-1000-HCl, a sign of successful reaction between boron-containing chemicals with HCl (Figure S28).[36] In

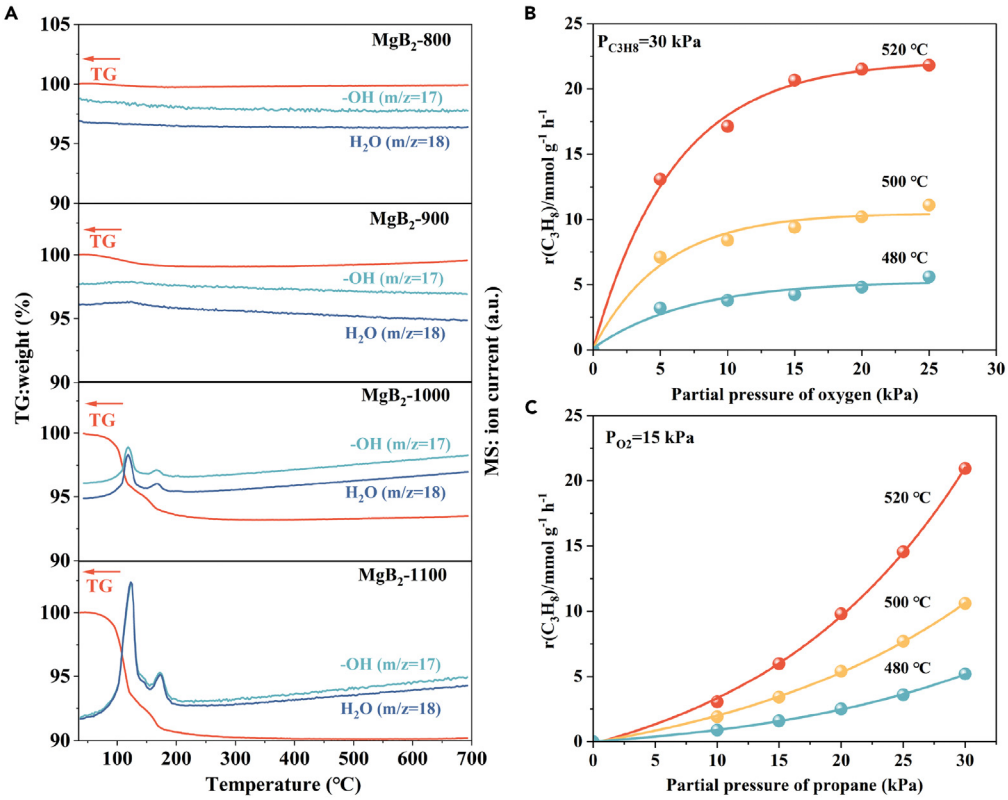

Figure 4. TG-MS characterizations and reaction order analyses over the catalysts

(A) TG-MS analysis under N_2 atmosphere.

(B and C) Reaction rate as a function of the partial pressure of (B) oxygen and (C) propane at 480°C, 500°C, 520°C in the ODHP over MgB_2-1000, balanced by N_2, WHSV = 12000 mL/g/h, 0.1MPa.

addition, the Brunauer-Emmett-Teller (BET) surface area of MgB_2-1000-HCl is 102.7 m^2g^{-1}, much higher than the untreated MgB_2-1000 (6.8 m^2g^{-1}) (Figure S29). Moreover, as shown in Figure S30, MgB_2-1000-HCl possesses a much higher pore volume (0.21 cm^3g^{-1}) than MgB_2-1000 (0.013 cm^3g^{-1}). Therefore, MgB_2-1000-HCl can provide more effective channels for gas diffusion and larger surface area for surface reaction, which is advantageous for ODHP.

The prepared MgB_2-1000-HCl catalyst was tested for ODHP. The activity of MgB_2-1000-HCl reached 38% at 520°C within 200 min, with a short activation period (Figure S31). This phenomenon is consistent with XPS results (Figure S32). Upon exposure to the reaction conditions, the peaks <190 eV (assigned to B-H) became weak but the peak at 192.8 eV (assigned to B-O) increased, which proves surface B-H became coordinated to oxygen over the reaction process,[37] and turned into active sites. Besides, the disappearance of B-H stretching mode in the IR spectrum of MgB_2-1000-HCl-Spent also proves this point (Figure S28). These results further confirmed that the BO_x was the active sites over MgB_2-1000-HCl catalyst. In addition, the TG-MS further exhibited that the fresh MgB_2-1000-HCl was easily oxidized (Figure S33A). However, the spent MgB_2-1000-HCl exhibited the oxidation-resistance properties, which indicates the catalyst could reach a stable structure during the reaction process (Figure S33B).

As shown in Figure 5A, because most of the inactive $Mg_2B_2O_5$ was excluded and the MgB_2-1000-HCl has the larger surface area, the catalytic performance of MgB_2-1000-HCl outperformed the untreated MgB_2-1000. The higher the reaction temperature, the greater the difference. MgB_2-1000-HCl was with slightly higher activation energy (E_a) for the ODHP reaction (Figure 5B), and therefore it requires higher temperatures to better show its full potential. Most importantly, the MgB_2-1000-HCl also retained excellent stability at 520°C. As shown in Figure 5C, the propane conversion was still around 38% and the olefins selectivity was maintained above 80% even after 100 h. Meanwhile, the carbon balance stayed at 100 $\pm$ 3% during the test (Figure S34). The XRD pattern of MgB_2-1000-HCl-Spent was also consistent with the fresh sample, indicating the activation indeed happened in the amorphous phase (Figure S35). By adjusting the catalytic tests with different feed gas (C_3H_8: O_2) ratios, as high as 60% propane conversion was achieved for MgB_2-1000-HCl at 535°C (Figure S36A). Meanwhile, the selectivities of propylene and ethylene were 47.8% and 24.7%, respectively, resulting in the maximum olefins yield of 43.2% at 535°C (Figure S36B). Moreover, the sample showed great long-term stability, measured at 535°C for 50 h. As shown in Figure S36C, the propane conversion was always around 60% and the olefins selectivity was maintained above 70%, with the carbon balance kept at 100 $\pm$ 3% during the test (Figure S36D). Compared with other typical boron-based catalysts for ODHP (Figure 5D), there is a rare precedent that boron-based catalysts can work long time at a high propane conversion (>35%). Although Zhou et al.[8] reported BS-1 catalyst exhibited a 43.7% propane

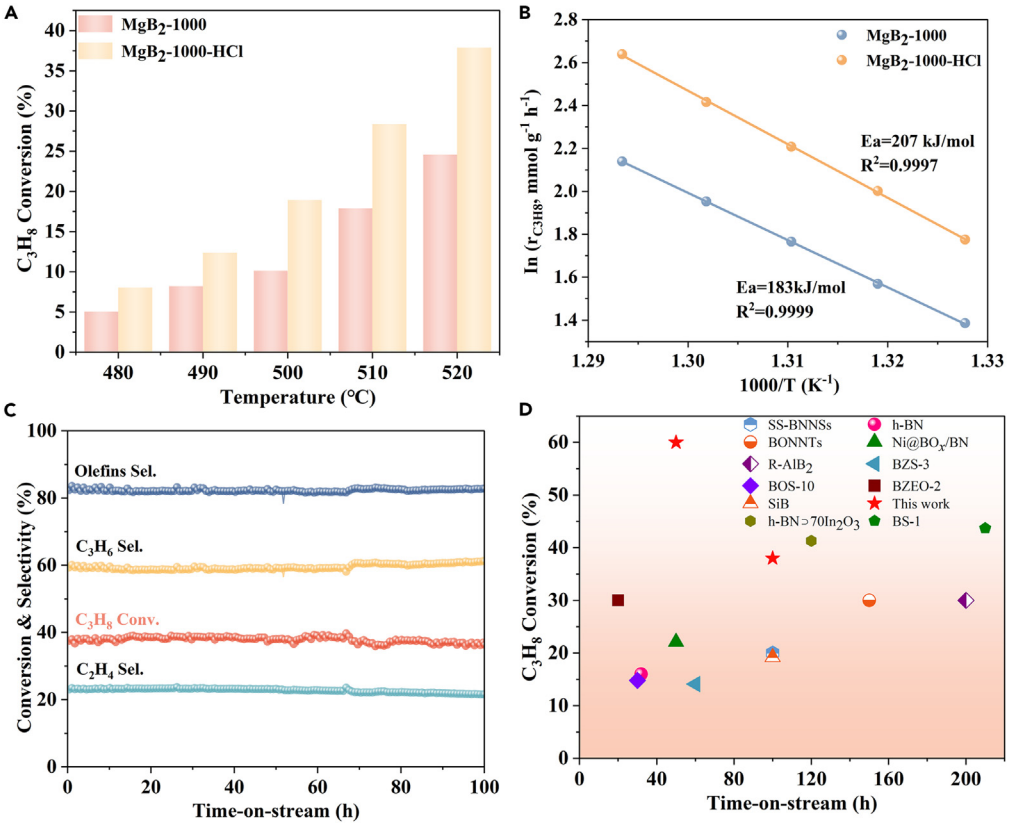

Figure 5. Catalytic evaluation of MgB_2-1000-HCl

(A) Propane conversion as a function of reaction temperature over MgB_2-1000 and MgB_2-1000-HCl.

(B) Arrhenius plots.

(C) Stability test during 100 h operation at 520°C over MgB_2-1000-HCl.

(D) Comparison of MgB_2-1000-HCl with the established OPDH catalysts at their reported stabilized state. See Table S2 for specific values. Reaction conditions: 0.1MPa, $C_3H_8/O_2/N_2$ ratio = 6:3:11, WHSV = 12000 mL/g/h.

conversion over 210 h and Cao et al.[19] reported h-BN⊃70In_2O_3 showed a 41.3% propane conversion over 120 h, the reaction temperatures were harsh: 570°C and 566°C, respectively. Therefore, the catalyst of MgB_2-1000-HCl with the excellent stability at a high propane conversion of 60% possesses huge potential for actual large-scale industrial production.

The excellent catalytic stability of MgB_2-1000-HCl motivated our investigation of the structure. As illustrated in Figure 6A, the basic coordination modes of B atoms with O atoms include BO_3 plane triangle (including six-membered boroxol ring and nonring BO_3) and BO_4 tetrahedron, respectively, defined as B-O ring, $B_{(3)}$-O and $B_{(4)}$-O, which are bound together in various ways to form multifunctional boron-oxygen network (BO_x).[38–41] The existence of $B_{(3)}$-O (1380 cm^{-1}) and $B_{(4)}$-O (1078 cm^{-1}) vibrations were identified in MgB_2-1000-HCl using FT-IR spectroscopy (Figure S28). Interestingly, after tested for ODHP reaction, the vibration intensity of $B_{(4)}$-O was significantly decreased but that of $B_{(3)}$-O was increased. It is noteworthy that a new peak was formed at 1240 cm^{-1}, which might be ascribed to B-O ring.[42,43] Thus, we speculate that $B_{(4)}$-O could be transformed into $B_{(3)}$-O and B-O ring under the high-temperature reaction process. To further prove the point, we investigated the structures of MgB_2-1000-HCl fresh and spent with ^{11}B magic angle spinning (MAS) nuclear magnetic resonance (NMR) spectroscopy. The spectra of MgB_2-1000-HCl-Fresh could be classified into two boron species $B_{(3)}$-O and $B_{(4)}$-O with chemical shifts at 11.8 and −3.2 ppm, respectively (Figure 6B). No boroxol ring was detected in the fresh sample, consistent with the FT-IR result. In contrast, the new peak appeared at 17.7 ppm in the spectrum of MgB_2-1000-HCl-Spent (Figure 6C), which could be assigned to boroxol ring.[44–46] The relative abundance of the three types of boron species for fresh and spent catalysts was summarized in Table S3. It can be seen the B-O ring was increased at the cost of $B_{(3)}$-O and $B_{(4)}$-O. Considering the fact that propane conversion increased from 8% to 38% during the reaction process (Figure S31), it can be inferred that there were dynamic transformations among the three boron species and the boroxol ring was vital for the high conversion of propane under harsh reaction conditions over MgB_2-1000-HCl.

Conclusions

We converted the inactive commercial MgB_2 into high-performance catalysts for ODHP by a simple thermal treatment in air. Surface BO_x anchored on $Mg_2B_2O_5$ crystallites produced by oxidizing MgB_2 under high temperatures was found to be the active site for propane

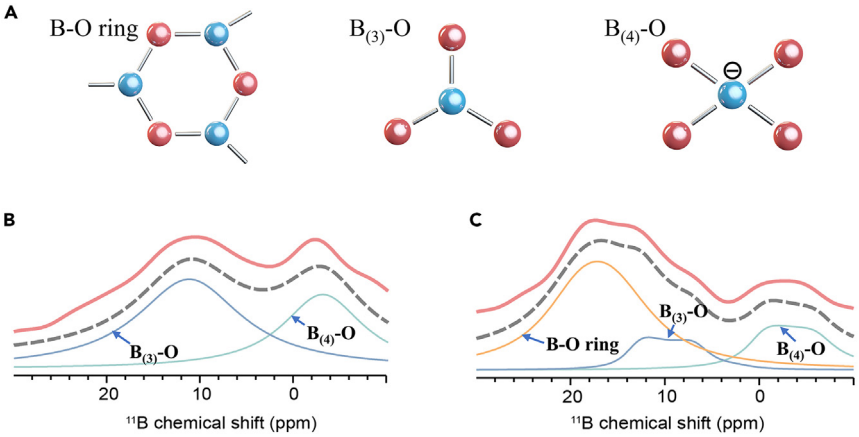

Figure 6. Schematic illustration of the different boron species and ^{11}B MAS NMR spectra characterization

(A) The proposed structure of the three types of boron species in the catalysts.

(B) ^{11}B MAS NMR spectra of MgB_2-1000-HCl-Fresh.

(C) ^{11}B MAS NMR spectra of MgB_2-1000-HCl-Spent. The solid lines represent the experimental spectra and the gray dashed lines represent the total analytical simulations of the spectra.

oxidation. This self-evolved catalyst prevailed over supporting BO_x on MgO for stabilizing the active sites. Moreover, the improved sample MgB_2-1000-HCl produced by simply treating MgB_2-1000 with HCl shows an unprecedented long-term high conversion of 60% with a high olefin yield of 43.2% at 535°C, which outstands from metal-based catalysts and common boron-based catalysts. It shows high resistance against deactivation by water, and even after the extreme treatment of immersing MgB_2-1000 in water, it did not lose its impressive catalytic performance. Furthermore, we dived into the molecular scale and pinpointed the B-O rings as the active sites by ^{11}B MAS solid-state NMR, kinetics study, and FT-IR characterizations. As it is said "simplicity is the ultimate sophistication", this new strategy of deriving advanced catalytic structure with simple treatments is friendly for scalable preparation of the catalyst for practical industrial production, and our journey to locate the active component and further improve the catalyst provides useful guidance for catalysts design at large.

Limitations of the study

Despite that the Mg-1000-HCl catalyst exhibits higher propane conversion than Mg-1000, the obtained mass of Mg-1000-HCl is lower due to the acid etching step. In addition, the gas-phase radical pathways of ODHP reaction for MgB_2-1000 are proposed but not directly probed. Therefore, future research work can further improve the atom efficiency and illustrate the pathways with more advanced probing instruments and experimental setups.

STAR★METHODS

Detailed methods are provided in the online version of this paper and include the following:

- KEY RESOURCES TABLE
- RESOURCE AVAILABILITY
  - Lead contact
  - Materials availability
  - Data and code availability
- METHOD DETAILS
  - Materials
  - Synthesis of MgB_2-x (x = 800, 900, 1000, 1100) catalysts
  - Synthesis of $Mg_2B_2O_5$ nanowires
  - Synthesis of B_2O_3/MgO and B_2O_3/MgO-800
  - Synthesis of MgB_2-1000-HCl
  - Catalysts performance evaluation
  - Characterization

SUPPLEMENTAL INFORMATION

Supplemental information can be found online at https://doi.org/10.1016/j.isci.2023.108135.

ACKNOWLEDGMENTS

The authors acknowledge the support from the Fundamental Research Funds for the Central Universities (226-2022-00159, 226-2022-00200), the National Natural Science Foundation of China (52372233, 61721005), and the U of T-ZJU Joint Seed Fund.

AUTHOR CONTRIBUTIONS

D.Z. and W.S. conceived the idea. D.Z. carried out the synthesis and catalysis experiments, analyzed the data, and prepared the manuscript under the supervision of W.S. and D.Y.

S.W. carried out the ICP and FT-IR experiments. X.L. carried out the ^{11}B(MAS) solid-state NMR characterization and analysis. C.Z., K.F., and L.H. carried out the TEM characterization and analysis. H.Z. carried out the FTIR experiments. All authors commented on the final manuscript.

DECLARATION OF INTERESTS

The authors applied for a Chinese patent during the preparation of the draft, and the patent was granted during the revision of the manuscript.

Received: July 27, 2023
Revised: August 8, 2023
Accepted: October 2, 2023
Published: October 6, 2023

REFERENCES

1. Sheng, J., Yan, B., Lu, W.D., Qiu, B., Gao, X.Q., Wang, D., and Lu, A.H. (2021). Oxidative dehydrogenation of light alkanes to olefins on metal-free catalysts. Chem. Soc. Rev. *50*, 1438–1468. https://doi.org/10.1039/d0cs01174f.
2. Grant, J.T., Venegas, J.M., McDermott, W.P., and Hermans, I. (2018). Aerobic oxidations of light alkanes over solid metal oxide catalysts. Chem. Rev. *118*, 2769–2815. https://doi.org/10.1021/acs.chemrev.7b00236.
3. Xing, F., Nakaya, Y., Yasumura, S., Shimizu, K.-I., and Furukawa, S. (2022). Ternary platinum–cobalt–indium nanoalloy on ceria as a highly efficient catalyst for the oxidative dehydrogenation of propane using CO_2. Nat. Catal. *5*, 55–65. https://doi.org/10.1038/s41929-021-00730-x.
4. Zhao, D., Tian, X., Doronkin, D.E., Han, S., Kondratenko, V.A., Grunwaldt, J.D., Perechodjuk, A., Vuong, T.H., Rabeah, J., Eckelt, R., et al. (2021). In situ formation of ZnOx species for efficient propane dehydrogenation. Nature *599*, 234–238. https://doi.org/10.1038/s41586-021-03923-3.
5. Ryoo, R., Kim, J., Jo, C., Han, S.W., Kim, J.C., Park, H., Han, J., Shin, H.S., and Shin, J.W. (2020). Rare-earth-platinum alloy nanoparticles in mesoporous zeolite for catalysis. Nature *585*, 221–224. https://doi.org/10.1038/s41586-020-2671-4.
6. Huang, Z., He, D., Deng, W., Jin, G., Li, K., and Luo, Y. (2023). Illustrating new understanding of adsorbed water on silica for inducing tetrahedral cobalt(II) for propane dehydrogenation. Nat. Commun. *14*, 100. https://doi.org/10.1038/s41467-022-35698-0.
7. Zhang, Z., Tian, H., Sun, J., Meira, D.M., Zhang, M., Ding, X., Ji, D., Qiu, C., Lu, Z., Sun, L., et al. (2023). Light-enabled coupling of tandem ethane dehydrogenation and CO_2 hydrogenation. Chem Catal. *3*, 100644. https://doi.org/10.1016/j.checat.2023.100644.
8. Zhou, H., Yi, X., Hui, Y., Wang, L., Chen, W., Qin, Y., Wang, M., Ma, J., Chu, X., Wang, Y., et al. (2021). Isolated boron in zeolite for oxidative dehydrogenation of propane. Science *372*, 76–80. https://doi.org/10.1126/science.abe7935.
9. Grant, J.T., Carrero, C.A., Goeltl, F., Venegas, J., Mueller, P., Burt, S.P., Specht, S.E., McDermott, W.P., Chieregato, A., and Hermans, I. (2016). Selective oxidative dehydrogenation of propane to propene using boron nitride catalysts. Science *354*, 1570–1573. https://doi.org/10.1126/science.aaf7885.
10. Liu, Y., Feng, W., Li, T., He, H., Dai, W., Huang, W., Cao, Y., and Fan, K. (2006). Structure and catalytic properties of vanadium oxide supported on mesocellulous silica foams (MCF) for the oxidative dehydrogenation of propane to propylene. J. Catal. *239*, 125–136. https://doi.org/10.1016/j.jcat.2005.12.028.
11. Kondratenko, E.V., Buyevskaya, O.V., and Baerns, M. (2001). Characterisation of vanadium-oxide-based catalysts for the oxidative dehydrogenation of propane to propene. Top. Catal. *15*, 175–180. https://doi.org/10.1023/A:1016649731881.
12. Stern, D.L., and Grasselli, R.K. (1997). Propane oxydehydrogenation over molybdate-based catalysts. J. Catal. *167*, 550–559. https://doi.org/10.1006/jcat.1997.1568.
13. Liu, Z., Yan, B., Meng, S., Liu, R., Lu, W.D., Sheng, J., Yi, Y., and Lu, A.H. (2021). Plasma tuning local environment of hexagonal boron nitride for oxidative dehydrogenation of propane. Angew. Chem. Int. Ed. *60*, 19691–19695. https://doi.org/10.1002/anie.202106713.
14. Cao, L., Dai, P., Tang, J., Li, D., Chen, R., Liu, D., Gu, X., Li, L., Bando, Y., Ok, Y.S., et al. (2020). Spherical superstructure of boron nitride nanosheets derived from boron-containing metal-organic frameworks. J. Am. Chem. Soc. *142*, 8755–8762. https://doi.org/10.1021/jacs.0c01023.
15. Love, A.M., Thomas, B., Specht, S.E., Hanrahan, M.P., Venegas, J.M., Burt, S.P., Grant, J.T., Cendejas, M.C., McDermott, W.P., Rossini, A.J., and Hermans, I. (2019). Probing the transformation of boron nitride catalysts under oxidative dehydrogenation conditions. J. Am. Chem. Soc. *141*, 182–190. https://doi.org/10.1021/jacs.8b08165.
16. Li, P., Zhang, X., Wang, J., Xue, Y., Yao, Y., Chai, S., Zhou, B., Wang, X., Zheng, N., and Yao, J. (2022). Engineering O-O species in boron nitrous nanotubes increases olefins for propane oxidative dehydrogenation. J. Am. Chem. Soc. *144*, 5930–5936. https://doi.org/10.1021/jacs.1c13563.
17. Love, A.M., Cendejas, M.C., Thomas, B., McDermott, W.P., Uchupalanun, P., Kruszynski, C., Burt, S.P., Agbi, T., Rossini, A.J., and Hermans, I. (2019). Synthesis and characterization of silica-supported boron oxide catalysts for the oxidative dehydrogenation of propane. J. Phys. Chem. C *123*, 27000–27011. https://doi.org/10.1021/acs.jpcc.9b07429.
18. Chaturbedy, P., Ahamed, M., and Eswaramoorthy, M. (2018). Oxidative dehydrogenation of propane over a high surface area boron nitride catalyst: exceptional selectivity for olefins at high conversion. ACS Omega *3*, 369–374. https://doi.org/10.1021/acsomega.7b01489.
19. Cao, L., Yan, P., Wen, S., Bao, W., Jiang, Y., Zhang, Q., Yu, N., Zhang, Y., Cao, K., Dai, P., and Xie, J. (2023). Antiexfoliating h-BN⊃In_2O_3 catalyst for oxidative dehydrogenation of propane in a high-temperature and water-rich environment. J. Am. Chem. Soc. *145*, 6184–6193. https://doi.org/10.1021/jacs.2c12136.
20. Zhang, X., You, R., Wei, Z., Jiang, X., Yang, J., Pan, Y., Wu, P., Jia, Q., Bao, Z., Bai, L., et al. (2020). Radical chemistry and reaction mechanisms of propane oxidative dehydrogenation over hexagonal boron nitride catalysts. Angew. Chem. Int. Ed. *59*, 8042–8046. https://doi.org/10.1002/anie.202002440.
21. Cheng, X., Zhang, Y., Wang, J., Zhang, X., Sun, C., Yang, Y., and Wang, X. (2023). B–O oligomers or ring species in AlB_2: which is more selective for propane oxidative dehydrogenation? ACS Catal. *13*, 1630–1637. https://doi.org/10.1021/acscatal.2c04889.

22. Storti, E., Roso, M., Modesti, M., Aneziris, C.G., and Colombo, P. (2016). Preparation and morphology of magnesium borate fibers via electrospinning. J. Eur. Ceram. Soc. *36*, 2593–2599. https://doi.org/10.1016/j.jeurceramsoc.2016.02.049.
23. Kipcak, A.S., Yildirim, M., Aydin Yuksel, S., Moroydor Derun, E., and Piskin, S. (2014). The synthesis and physical properties of magnesium borate mineral of admontite synthesized from sodium borates. Adv. Mater. Sci. Eng. *2014*, 1–9. https://doi.org/10.1155/2014/819745.
24. Grant, J.T., McDermott, W.P., Venegas, J.M., Burt, S.P., Micka, J., Phivilay, S.P., Carrero, C.A., and Hermans, I. (2017). Boron and boron-containing catalysts for the oxidative dehydrogenation of propane. ChemCatChem *9*, 3623–3626. https://doi.org/10.1002/cctc.201701140.
25. Chen, K., Wang, Z., Wang, L., Wu, X., Hu, B., Liu, Z., and Wu, M. (2021). Boron nanosheet-supported Rh catalysts for hydrogen evolution: a new territory for the strong metal-support interaction effect. Nano-Micro Lett. *13*, 138. https://doi.org/10.1007/s40820-021-00662-y.
26. Hou, C., Tai, G., Hao, J., Sheng, L., Liu, B., and Wu, Z. (2020). Ultrastable crystalline semiconducting hydrogenated borophene. Angew. Chem. Int. Ed. *59*, 10819–10825. https://doi.org/10.1002/anie.202001045.
27. Xiao, L., Li, X., Zhang, J., and He, Z. (2021). MgB_4 MXene-like nanosheets for photocatalytic hydrogen evolution. ACS Appl. Nano Mater. *4*, 12779–12787. https://doi.org/10.1021/acsanm.1c03497.
28. Wan, Y., Samundsett, C., Bullock, J., Hettick, M., Allen, T., Yan, D., Peng, J., Wu, Y., Cui, J., Javey, A., and Cuevas, A. (2016). Conductive and stable magnesium oxide electron-selective contacts for efficient silicon solar cells. Adv. Energy Mater. *7*, 1601863. https://doi.org/10.1002/aenm.201601863.
29. Song, T., Li, R., Wang, J., Dong, C., Feng, X., Li, S., Mu, R., and Fu, Q. (2023). Selective oxidation of methane to CO on Ni@BOx via reaction-induced vapor migration of boron-containing species onto Ni. Appl. Catal., B *321*, 122021. https://doi.org/10.1016/j.apcatb.2022.122021.
30. Guo, Y., Zhang, W., Yang, D., Yao, R.-L., and Naslain, R. (2012). Decomposition and Oxidation of Magnesium Diboride. J. Am. Ceram. Soc. *95*, 754–759. https://doi.org/10.1111/j.1551-2916.2011.04998.x.
31. Gao, B., Qiu, B., Zheng, M., Liu, Z., Lu, W.-D., Wang, Q., Xu, J., Deng, F., and Lu, A.-H. (2022). Dynamic Self-Dispersion of Aggregated Boron Clusters into Stable Oligomeric Boron Species on MFI Zeolite Nanosheets under Oxidative Dehydrogenation of Propane. ACS Catal. *12*, 7368–7376. https://doi.org/10.1021/acscatal.2c01622.
32. Qiu, B., Jiang, F., Lu, W.-D., Yan, B., Li, W.-C., Zhao, Z.-C., and Lu, A.-H. (2020). Oxidative dehydrogenation of propane using layered borosilicate zeolite as the active and selective catalyst. J. Catal. *385*, 176–182. https://doi.org/10.1016/j.jcat.2020.03.021.
33. Yan, B., Li, W.-C., and Lu, A.-H. (2019). Metal-free silicon boride catalyst for oxidative dehydrogenation of light alkanes to olefins with high selectivity and stability. J. Catal. *369*, 296–301. https://doi.org/10.1016/j.jcat.2018.11.014.
34. Venegas, J.M., Zhang, Z., Agbi, T.O., McDermott, W.P., Alexandrova, A., and Hermans, I. (2020). Why boron nitride is such a selective catalyst for the oxidative dehydrogenation of propane. Angew. Chem. Int. Ed. *59*, 16527–16535. https://doi.org/10.1002/anie.202003695.
35. Tian, J., Tan, J., Xu, M., Zhang, Z., Wan, S., Wang, S., Lin, J., and Wang, Y. (2019). Propane oxidative dehydrogenation over highly selective hexagonal boron nitride catalysts: The role of oxidative coupling of methyl. Sci. Adv. *5*, eaav8063. https://doi.org/10.1126/sciadv.aav8063.
36. Nishino, H., Fujita, T., Cuong, N.T., Tominaka, S., Miyauchi, M., Iimura, S., Hirata, A., Umezawa, N., Okada, S., Nishibori, E., et al. (2017). Formation and characterization of hydrogen boride sheets derived from MgB_2 by cation exchange. J. Am. Chem. Soc. *139*, 13761–13769. https://doi.org/10.1021/jacs.7b06153.
37. Kawamura, R., Cuong, N.T., Fujita, T., Ishibiki, R., Hirabayashi, T., Yamaguchi, A., Matsuda, I., Okada, S., Kondo, T., and Miyauchi, M. (2019). Photoinduced hydrogen release from hydrogen boride sheets. Nat. Commun. *10*, 4880. https://doi.org/10.1038/s41467-019-12903-1.
38. Kroeker, S., and Stebbins, J.F. (2001). Three-coordinated boron-11 chemical shifts in borates. Inorg. Chem. *40*, 6239–6246. https://doi.org/10.1021/ic010305u.
39. Shi, Z.H., Chi, Y., Yang, M., Liu, W., and Guo, S.P. (2020). A series of chalcogenide borates $RE_6Ta_2MgQB_8O_{26}$ (RE = Sm, Eu, Gd; Q = S, Se) featuring a B_4O_{10} Cluster. Inorg. Chem. *59*, 3532–3536. https://doi.org/10.1021/acs.inorgchem.0c00086.
40. Youngman, R.E., and Zwanziger, J.W. (1995). On the formation of tetracoordinate boron in rubidium borate glasses. J. Am. Chem. Soc. *117*, 1397–1402. https://doi.org/10.1021/ja00109a026.
41. Huang, C., Mutailipu, M., Zhang, F., Griffith, K.J., Hu, C., Yang, Z., Griffin, J.M., Poeppelmeier, K.R., and Pan, S. (2021). Expanding the chemistry of borates with functional $[BO_2]^-$ anions. Nat. Commun. *12*, 2597. https://doi.org/10.1038/s41467-021-22835-4.
42. Chen, J.-Y., Wang, W.-L., Zhou, L.-J., and Pan, Z.-H. (2020). Effect of Al_2O_3 and MgO on crystallization and structure of $CaO–SiO_2–B_2O_3$-based fluorine-free mold flux. J. Iron Steel Res. Int. *28*, 552–562. https://doi.org/10.1007/s42243-020-00439-4.
43. Wang, W., Dai, S., Zhou, L., Zhang, J., Tian, W., and Xu, J. (2020). Viscosity and structure of $MgO–SiO_2$-based slag melt with varying B_2O_3 content. Ceram. Int. *46*, 3631–3636. https://doi.org/10.1016/j.ceramint.2019.10.082.
44. Yan, H., Alayoglu, S., Wu, W., Zhang, Y., Weitz, E., Stair, P.C., and Notestein, J.M. (2021). Identifying boron active sites for the oxidative dehydrogenation of propane. ACS Catal. *11*, 9370–9376. https://doi.org/10.1021/acscatal.1c02168.
45. Lee, S.K., Mibe, K., Fei, Y., Cody, G.D., and Mysen, B.O. (2005). Structure of B_2O_3 Glass at High Pressure: A 11B Solid-State NMR Study. Phys. Rev. Lett. *94*, 165507. https://doi.org/10.1103/PhysRevLett.94.165507.
46. Du, L.-S., and Stebbins, J.F. (2003). Nature of silicon−boron mixing in sodium borosilicate glasses: a high-resolution ^{11}B and ^{17}O NMR Study. J. Phys. Chem. B *107*, 10063–10076. https://doi.org/10.1021/jp034048l.

STAR★METHODS

KEY RESOURCES TABLE

REAGENT or RESOURCE	SOURCE	IDENTIFIER
Chemicals, peptides, and recombinant proteins		
Magnesium boride (99% trace metals basis)	Macklin	CAS:12007-25-9
Boron oxide (98% purity)	Macklin	CAS:1303-86-2
Potassium chloride (99.8% purity)	Macklin	CAS:7447-40-7
Boron silicide (99.5% purity)	Macklin	CAS:12007-81-7
Boron carbide (99.5% purity)	RHAWN	CAS:12069-32-8
Nickel boride (99% metals basis)	RHAWN	CAS:12007-00-0
Hydrochloric acid (36.0–38.0% purity)	Sinopharm Chemical Reagent Co., Ltd	CAS:7647-01-0
Sodium hydroxide (≥96.0% purity)	Sinopharm Chemical Reagent Co., Ltd	CAS:1310-73-2
Magnesium oxide (99% purity)	Sinopharm Chemical Reagent Co., Ltd	CAS:1309-48-4
Boric acid (≥99.50% purity)	Sinopharm Chemical Reagent Co., Ltd	CAS:10043-35-3
Boron nitride (99.9% metals basis)	TENSUS BIOTECH	CAS:10043-11-5
Magnesium chloride, hexahydrate(≥99.0% purity)	Aladdin	CAS:7791-18-6

RESOURCE AVAILABILITY

Lead contact

Further information and requests for resources should be directed to and will be fulfilled by the lead contact, Wei Sun (sunnyway423@zju.edu.cn)

Materials availability

All materials generated in this study are available from the lead contact without restriction.

Data and code availability

- The datasets and images generated during this study are available from the lead contact upon request.
- This paper does not report original code.
- Any additional information required to reanalyze the data reported in this paper is available from the lead contact upon request.

METHOD DETAILS

Materials

All the chemicals purchased were used without further purification. Magnesium diboride (MgB_2), Boron trioxide (B_2O_3), Potassium chloride (KCl), Boron silicide (SiB) were purchased from Macklin. Boron carbide (B_4C) and Nickel boride (NiB) were purchased from RHAWN. Hydrochloric acid (36%–38%, analytical reagent), Sodium hydroxide (NaOH), magnesium oxide (MgO) and Boric acid (H_3BO_3) were purchased from Sinopharm Chemical Reagent Co., Ltd. Boron nitride (h-BN) was purchased from Tensus Biotech. Magnesium chloride hexahydrate ($MgCl_2 \cdot 6H_2O$) was purchased from Aladdin. Milli-Q water (Millipore, 18.2 MΩ cm at 25°C) was used in all experiments.

Synthesis of MgB_2-x (x = 800, 900, 1000, 1100) catalysts

MgB_2-x catalysts were prepared by high temperature calcination in air. The purchased MgB_2 was put into a muffle furnace and calcined at x °C for 3 h with a ramp rate of 10°C/min.

Synthesis of $Mg_2B_2O_5$ nanowires

For a typical batch, $MgCl_2 \cdot 6H_2O$ (1.524 g), H_3BO_3 (0.463 g) and NaOH (0.6 g) were dissolved in 50 mL of deionized water under magnetic stirring at room temperature. The obtained product (denoted as reaction precursor) was washed with deionized water several times and dried in an oven. 0.2g of the obtained reaction precursor was mixed with 0.08g of H_3BO_3 and 0.4g of KCl. The mixed product was ground to powder, which was then transferred to a muffle furnace and calcined at 830°C for 5 h with a heating rate of 5°C/min. Finally, the calcined product was washed with deionized water several times and $Mg_2B_2O_5$ nanowires were obtained.

Synthesis of B_2O_3/MgO and B_2O_3/MgO-800

The sample was prepared by the conventional impregnation method using MgO as the support. 0.3g of B_2O_3 and 0.7g of MgO were dissolved in 20 mL of deionized water. After treatment with ultrasound for 20 min, the solvent of the mixed products was evaporated at 105°C under stirring (denoted as precursor). Then the precursor was calcined at 500°C for 3h (denoted as B_2O_3/MgO). Alternatively, the precursor was calcined at 800°C for 3h and the B_2O_3/MgO-800 was obtained.

Synthesis of MgB_2-1000-HCl

300 mg of MgB_2-1000 was dissolved in 10 mL of hydrochloric acid (36%–38%, analytical reagent). The mixed solution of MgB_2-1000 was transferred to a shaking bed (400 rpm, 50°C) and kept for 24 h. The obtained product (denoted as MgB_2-1000-HCl) was then washed with ethanol several times and dried in a vacuum oven.

Catalysts performance evaluation

All the catalysts were tested in a flow fixed-bed quartz reactor (I.D. = 6 mm, length = 50 cm) under atmospheric pressure. The catalysts were compressed and sieved to collect particles in 40–60 mesh. The catalysts (0.1g) were placed in the middle of the reactor and the reaction temperature was controlled by a thermocouple fixed in the inner part of the reactor and directly contacted with catalysts. The feed gases including C_3H_8, O_2, N_2 were controlled by mass flow controllers. The total flow rate was 20 mL/min. Before performance evaluation, there were no pretreatment procedures in the reactor. The reaction temperature was from 480°C to 530°C.

The reactants and products were analyzed by online gas chromatography (Agilent 8860) equipped with a thermal conductivity detector (TCD) to detect O_2, N_2, CO, CO_2, and a flame ionization detector (FID) to detect C_3H_8, C_3H_6, C_2H_6, C_2H_4, CH_4 et al. The conversion of propane and selectivity of products were calculated as follows[14,44]:

$$C_3H_8\ Conversion\ (\%) = \frac{C\ mol\ of\ (C_3H_{8,in} - C_3H_{8,out})}{C\ mol\ of\ C_3H_{8,in}} \times 100\% \quad \text{(Equation 1)}$$

$$Product\ selectivity\ (\%) = \frac{C\ mol\ of\ a\ certain\ product}{C\ mol\ of\ products} \times 100\% \quad \text{(Equation 2)}$$

$$Carbon\ Balance\ (\%) = \frac{C\ mol\ of\ (products + C_3H_{8,out})}{C\ mol\ of\ C_3H_{8,in}} \times 100\% \quad \text{(Equation 3)}$$

Where C mol represents the mole number of carbons in feed gases and effluent gases.

Characterization

The morphologies of the catalysts were analyzed by field emission scanning electron microscopy (SEM) (FEI, HITACHI S4800). Transmission electron microscopy (TEM) images were acquired on a FEI-Tecnai F20 (200 kv). Powder XRD patterns were measured on an XRD-700 (Shimadzu). The actual boron content of the catalysts was measured by an inductively coupled plasma optical emission spectroscopy (ICP-OES, Thermofisher). Fourier transform infrared spectroscopy (FT-IR) spectra were recorded by a Bruker Alpha FTIR spectrometer fitted with a universal attenuated total reflectance sampling accessory. X-ray photoelectron spectroscopy (XPS) analysis was performed using a Thermo Scientific k-Alpha equipped with an Al ka X-ray source (hv = 1486.6 eV) and binding energies referenced to C1s (284.8 eV). The Thermogravimetric analysis (TG) or Thermogravimetric and mass-spectrometric (TG-MS) was measured using STA449-QMS403 from NETZSCH. The specific surface areas of samples were measured using N_2 adsorption-desorption isotherms at −196°C on a TriStar II 3020 instrument from micromeritics. The samples were outgassed at 200°C before measurement.

^{11}B Solid-State NMR Spectroscopy was recorded on a Bruker 500 MHz widebore magnet spectrometer equipped with AVANCE *NEO* console and 1.3 mm HXY MAS probe configured in double-resonance mode. Direct excitation ^{11}B magic-angle spinning (MAS) spectra were collected with a MAS frequency of 60000 Hz at room temperature by using 1D spin echo sequence for suppression of background signals with a recycle delay of 5 s. SPINAL-64 1H heteronuclear decoupling was applied during signal acquisition with an RF field of 100 kHz. All experiments on the ^{11}B nucleus were referenced to the H_3BO_3 aqueous solution at 19.6 ppm and processed with the same Bruker Topspin window function parameters for quantitative comparison. Simulations of ^{11}B MAS NMR spectra were performed in the solid lineshape analysis (SOLA) module included in the Topspin 4.0 software.